The analysis of internal stresses on a welded joint in Grade 91 steel under creep test loading: Synchrotron X-ray diffraction measurements and modelling

Solenne Collomb, Xiaolei Chen, Jean-Philippe Tinnes, Thomas Schenk, Olivier Ferry, Svetlana Tsareva, Abdelkrim Redjaïmia, Alain Jacques

The analysis of internal stresses on a welded joint in Grade 91 steel under creep test loading: Synchrotron X-ray diffraction measurements and modelling

Solenne Collomb [a], Xiaolei Chen [b,c,d], Jean-Philippe Tinnes [a], Thomas Schenk [a,c,*], Olivier Ferry [a], Svetlana Tsareva [a], Abdelkrim Redjaïmia [a,c], Alain Jacques [a,c]

[a] Université de Lorraine, CNRS, IJL, F-54000 Nancy, France
[b] LEM3 Laboratory, Université de Lorraine, CNRS, Arts et Métiers ParisTech, F-57000 Metz, France
[c] LABoratoire d'EXcellence DAMAS, Université de Lorraine, F-57000, Metz, France
[d] Université Paris-Saclay, CentraleSupélec, ENS Paris-Saclay, CNRS, LMPS, Gif-sur-Yvette, France

ARTICLE INFO

Keywords:
In situ synchrotron XRD
Creep strain analysis
Welded joint
Grade 91
Kinetic
Modelling

ABSTRACT

The analysis and understanding of creep damage of Grade 91 steel welded joints is an important topic in the energy industry. Creep tests on welded joints were carried out at 600 °C, 100 MPa and then interrupted at 0%, 10%, 30%, 50%, 80% of the expected life and after failure. Creep damage is characterised by cavity bands located exclusively in the core of the sample in the InterCritical Heat Affected Zone (ICHAZ). These samples were tested using *in situ* synchrotron X-ray Diffraction (XRD) along the welded joint under creep conditions for the different creep times. The experimental results show a significant evolution of strain and creep damage characteristics on the welded joint, with a local maximum at the Heat Affected Zone (HAZ). Subsequently, a finite element creep strain analysis was performed for comparison with the experimental results.

1. Introduction

Martensitic steels such as Grade 91, 9Cr1Mo-NbV, are used to build components of thermal power plants. They indeed exhibit exceptional creep properties between 540 °C and 610 °C [1], after a fine-tuned heat treatment [2]. Welding is commonly used to join these Grade 91 power-plant components. However, this method leads to significant changes of their mechanical properties and also to an unusual damage mode near the welded joint. At high temperatures and low stresses, damage is present with cavities and a Type IV region fracture, localised in the Heat Affected Zone (HAZ), close to the base metal, *i.e.* the InterCritical Heat Affected Zone (ICHAZ) [3,4]. The ICHAZ microstructure is composed of coarse previous martensitic grains and new fine martensitic grains as well as a wide range of precipitates of different sizes. This heterogeneous zone is comparatively weaker than the other weld zones and accumulates creep damage in the form of creep voids. Different authors observe an initiation of cavities in the HAZ at about 20% of the lifetime. The number of cavities increases up to about 70% of the lifetime, then the cavities coalesce around 80% of the lifetime to form cracks [4,5]. Some authors focussed on the distribution of internal stresses in order to explain this cavitation phenomenon: the local concentration of plastic strain and the high triaxiality rate might influence the distribution of cavities [3,6]. The heterogeneity of the ICHAZ microstructure results in significant multiaxial stresses [4,7]. Ogata [6] conducted an internal pressure creep test on a longitudinal welded joint and reported that the higher voids number density is localised at the mid-thickness in the HAZ, where the circumferential stress and the stress triaxiality are highest. According to the authors, the heterogeneity in the welded joint affects the stress and strain distribution, which modifies the creep damage kinetics [8,9]. Multi-materials finite element calculations support this stress effect in the welded joint, except that the creep properties of each constituent have been only deduced from the base metal, which are not systematically determined by experiments [10]. Thus, it is necessary to determine the physical mechanisms responsible for the damage in each zone before modelling them (damage controlled by principal stress or Von Mises stress). The purpose of the present paper is thus to study the evolution of internal stresses during creep, and their influence on the initiation of the cavitation phenomenon is further investigated. For this purpose, we performed *in situ* synchrotron XRD tests along welded joint under creep conditions at different times of their creep life. Then a finite element creep strain analysis is conducted for comparison with the experimental results.

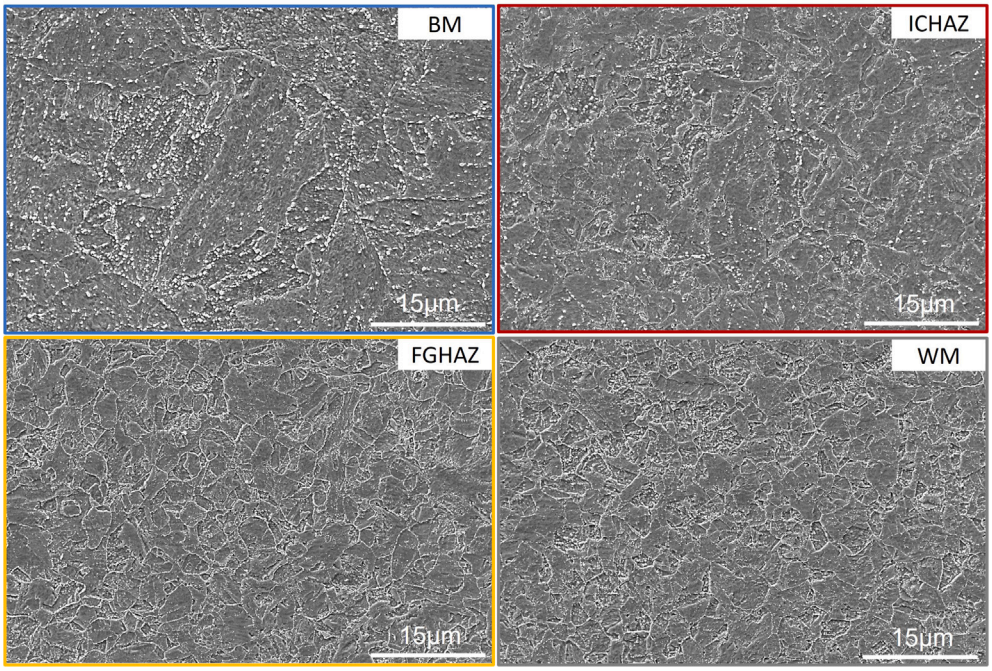

Fig. 1. SEM pictures of the welded joint microstructures for: base metal, HAZ with ICHAZ and FGHAZ, and the weld metal.

Table 1
Chemical composition of Grade 91 and Thermanit MTS-3 (wt%) welding wire.

Composition	C	Si	Mn	Cr	Mo	V	Nb	Ni	Cu	N
Base metal	0.11	0.31	0.51	8.5	0.97	0.20	0.07	0.07	0.03	0.04
Weld metal	0.10	0.29	0.5	9.7	0.93	0.19	0.06	0.4	0.03	0.04

2. Material and methods

2.1. Welding process

The chemical composition of ASTM Grade 91 (9Cr-1Mo-V-Nb) is shown in Table 1. The microstructure of that steel was obtained after an austenitisation at 1060 °C for 60 min, air cooling, then a tempering at 785 °C for 60 min. A chamfered 20 mm thick plate was multi-pass welded using the Tungsten Inert Gas process (TIG), with Thermanit MTS-3 welding wire (Table 1). The plate was pre-heated at 200 °C before the welding and maintained between 200 °C and 300 °C during the welding. A multi-layer welding was realised with 46 welding passes at 180 A and 8 mm/min. A post-weld heat treatment was applied at a temperature of 760 °C during 2 h to reduce the residual stresses created during the welding process. The joint weld consists of different parts, namely the weld metal, in the centre, surrounded by the heat affected zone (HAZ), followed by the base metal. The HAZ is divided in two zones, a Fine Grain HAZ (FGHAZ) and an intercritical heat affected zone (ICHAZ), located at the interface with the base metal. The corresponding microstructures of these different parts observed by Scanning Electron Microscope (SEM) are presented in Fig. 1. Because of the multi-pass welding, the coarse grain HAZ created during a pass was altered by the next pass, transforming the microstructure into fine grains. Cross-weld samples, with 8 mm diameter and a 50 mm gauge length were machined in the perpendicular direction of the welded joint in the plate, to have the weld metal in the centre of the sample.

2.2. Interrupted creep tests

Creep tests were performed on welded joints according to ISO 204. The temperature was controlled with 3 thermocouples to ensure homogeneity. The temperature gradient between the bottom and the top

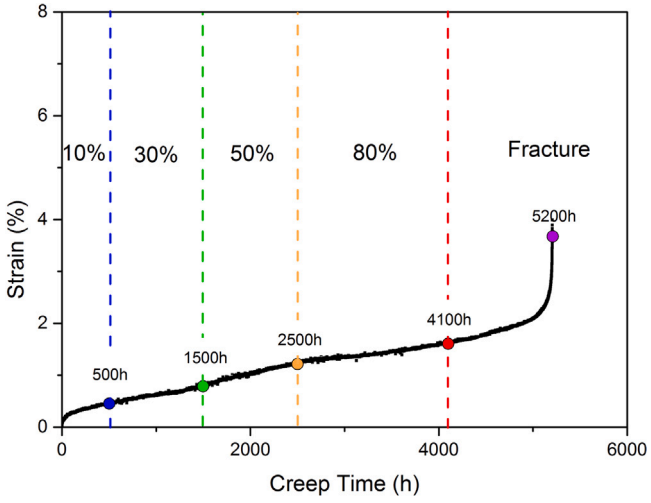

Fig. 2. Intermediate and failed creep tests of the welded joint sample, at 600 °C and 100 MPa.

of the furnace did not exceed +/−2 °C. The crossheads displacement was measured by two extensometers, on both heads of the sample. Temperature and stress levels have been chosen to lead to the same kind of damages as the ones observed in power plants pipes. Constant load creep tests were performed at 600 °C, 100 MPa, under controlled atmosphere. Several samples were tested under the same creep conditions (temperature and stress) and the tests were interrupted at respectively 0%, 10%, 30%, 50%, 80% of the expected lifetime and after fracture. With these creep conditions (600 °C and 100 MPa) the fracture occurs after 5200 h, as shown in Fig. 2.

2.3. Synchrotron XRD tests

The experiments were performed on the P21.2 Swedish materials science beamline of the DESY PETRA III synchrotron with a monochromatic beam energy of 89.59 ± 0.01 keV ($\Delta E/E = 2 \times 10^{-3}$). Such a

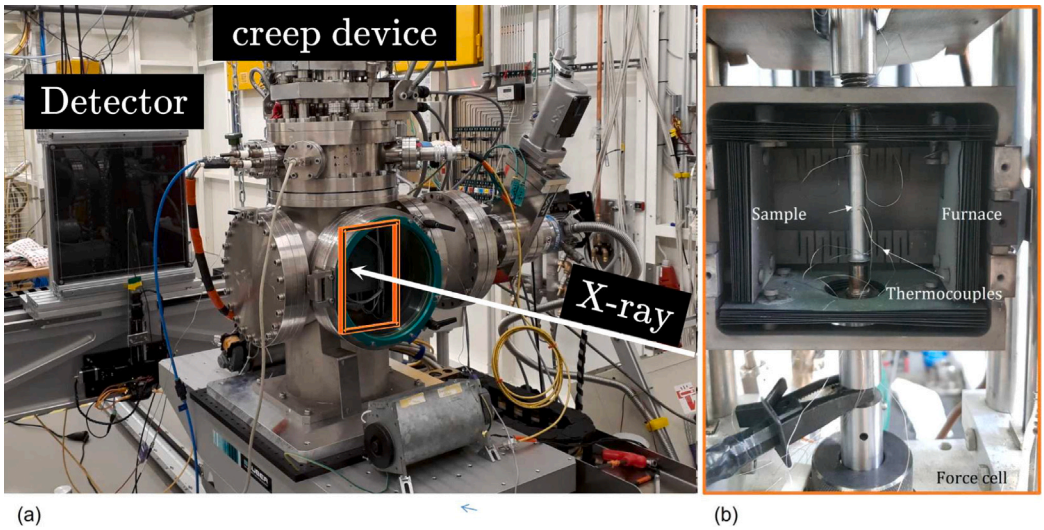

Fig. 3. (a) *in situ* testing device on beamline P21.2 at the DESY PETRA III synchrotron (Germany), with schematic X-ray beam path, (b) focus on testing device furnace, showing the sample with welded thermocouples.

high-energy synchrotron X-ray beamline provides a penetrating beam which allows diffraction experiments in transmission through an 8 mm thick specimen and thus to obtain volume information on massive samples. The diffraction rings were collected on a high-resolution 2048 × 2048 flat panel Perkin-Elmer detector with a 150 × 150 μm pixels size at a distance of 916.47 ± 0.2 mm from the specimen axis. To determinate internal residual stresses, the five pre-crept samples were strained at 600 °C and 100 MPa (creep conditions) for two hours in a high temperature tensile device [11] transparent to X-rays which had been put on a heavy load diffractometer (Fig. 3). Successive diffraction patterns were then recorded every 100 μm along the gauge length of the specimen (50 mm). Two specimen orientations were used (Fig. 5): 0° (resp. 90°) orientation, for which the incident beam is oriented along the X1 (resp. X2) axis. In the first case the incident beam travels through homogeneous areas of the specimen, while in the second one it travels through areas with a different microstructure and stress state. The resulting diffracted rings are collected along the beam path through the specimens.

Debye–Scherrer rings were corrected with a dark field image and calibrated, using the pyFAI software [12]. These diffraction patterns were sliced into ninety 4° wide azimuthal sectors. These sectors were then integrated to obtain ninety diffractograms. A diffractogram of a sector is the integrated intensity as function of the diffraction angle 2θ. All diffractograms were fitted with Pearson VII functions, to precisely measure the 2θ angular position variations of the diffraction peaks (Fig. 4). To remove uncertainties due to the variations of the beam position over time, averaging of opposite azimuths was used.

The $\sin^2\Psi$ method is used to determinate the internal residual stresses with the XRD experiments, as it is sensitive to small variations [13,14]. The angles (Ψ, Φ, θ, δ) used for this method are defined in the scheme Fig. 5 (a), by equations [14–16]:

$$\sin^2\Psi = 1 - (\cos\Phi^2\sqrt{(1-\sin^2\delta)}) \tag{1}$$

with 2θ the peak position and δ the azimuth angle on the Debye–Scherrer ring. In the case of triaxial stress state, the measured strain $\varepsilon_{\Psi\Phi}$ is the tensor projection on the measurement direction $\boldsymbol{n}$, defined by:

$$\begin{aligned}\varepsilon_{\Psi\Phi} &= \boldsymbol{n}\boldsymbol{\varepsilon}\boldsymbol{n}^t \\ &= \sin^2\Psi\cos^2\Phi\varepsilon_{11} + \sin^2\Psi\sin^2\Phi\varepsilon_{22} + \cos^2\Psi\varepsilon_{33} + \sin^2\Psi\sin 2\Phi\varepsilon_{12} \\ &+ \sin 2\Psi\sin\Phi\varepsilon_{23} + \sin 2\Psi\cos\Phi\varepsilon_{13}\end{aligned}$$

with $\epsilon_{ij} = \frac{1+\nu}{E}\sigma_{ij} - \frac{\nu}{E}\delta_{ij}\sigma_{kk}$ and $\delta_{ij} = 1$ if $i = j$ or 0 if $i \neq j$. Peak fitting was focussed on the {211} peak (see Fig. 4b) because the radiocrystallographic elastic constants of the {211} peak are representative of macroscopic constants [14].

3. Experimentals results

3.1. Type IV cracking

A creep test was carried out at 600 °C and 100 MPa until failure at 5200 h. The sample fracture occurred in the HAZ and more especially at ICHAZ, close to the base metal and parallel to the fusion line (see Fig. 6). This Type IV fracture is produced by creep cavitation. The fracture zone exhibits a significant necking which is also apparent in the second HAZ of the welded joint, with less area reduction. This necking suggests a high local viscoplastic deformation, which started during stage II of creep and increased during stage III. The major part of the specimen elongation results from this local strain.

3.2. Cavities

The optical micrographs in Fig. 6 show the two necking zones of the fractured sample. A high density of cavities is observed along the fracture and in the second ICHAZ. These cavity bands are located exclusively in the core of the sample and not on the surface. The SEM pictures in Fig. 6 indicate that these cavities were intergranular and appeared mainly in the vicinity of prior austenite grain boundaries. There are three categories of cavities as pointed out by the SEM pictures: small isolated cavities between the grains, clusters of connected medium sized cavities and finally a coalescence of cavities that form the nuclei of cracks. The crack tips at grain boundaries are blunted. However, despite the high local strain, the grains near the cavities do not seem distorted. Thus, the cavities nucleation was not only due to the viscoplastic deformation. These observations justify the analyses of internal stress distributions to explain the occurrence of these cavities. The SEM characterisation shows that cavities are clustered in a band located at 2 mm from the fusion line *i.e.*, in the ICHAZ, close to the base metal. This band is only present in the core of the sample, relatively far from the surface. Cavitation damage starts during stage II of creep (20%–30% of the lifetime), with the presence of a low density of small cavities. Then, a band of cavities appears from 2500 h (50% of lifetime) and increases in density with creep time. The cavities size drastically increases from 4100 h, *i.e.* during stage III creep. These results are in agreement with Li [4].

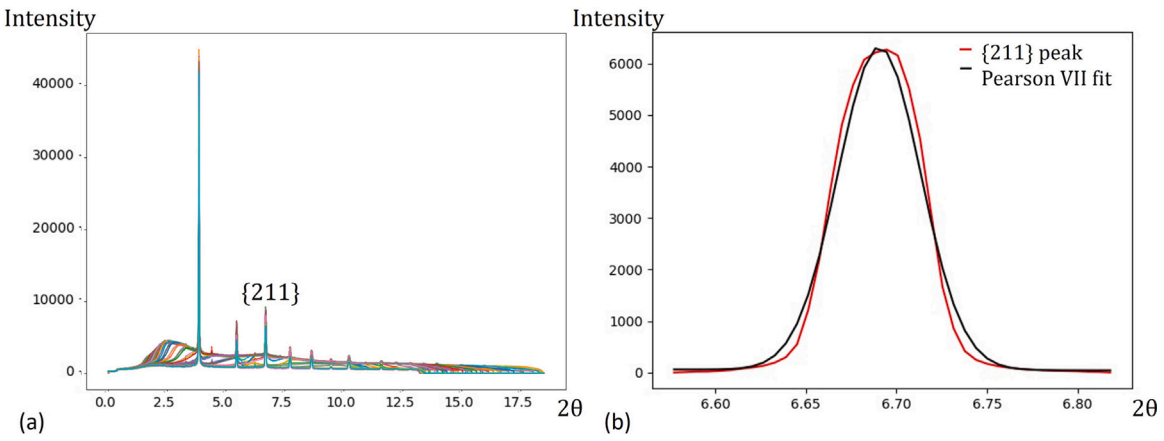

Fig. 4. (a) Diffractogram of intensity as function of Bragg diffraction angle 2θ, for one position on the welded joint and for the 90 sectors of the diffraction rings. (b) Focus on the peak 211 with Pearson VII fit.

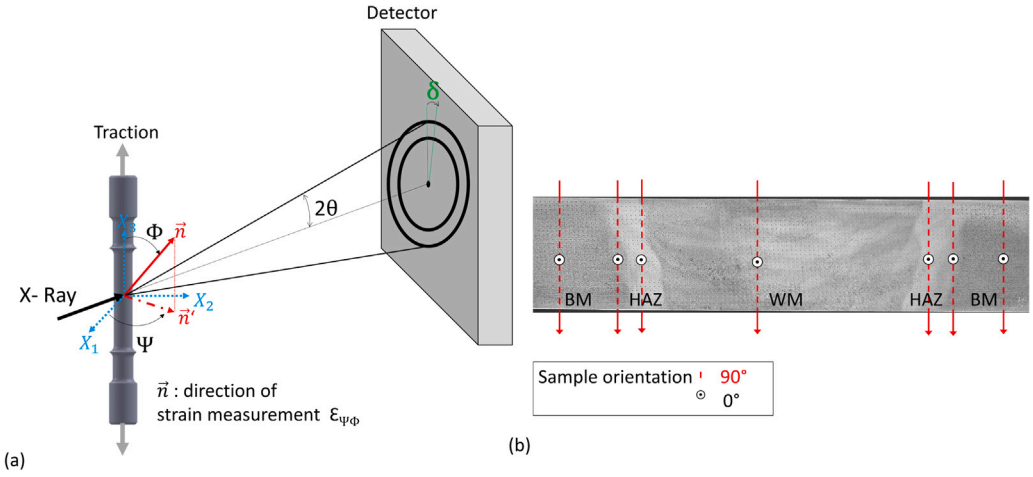

Fig. 5. (a) Illustration of the direction and angles of strain measurement for an XRD test, (b) the optical micrograph of the welded joint, crossed by the X-ray beam for the 0° and 90° specimen orientation.

3.3. Internal elastic strain monitoring during creep life

In our case, for a 0° (90°) sample orientation the strain equation $\varepsilon_{\Psi\Phi}$ becomes:

$$\varepsilon_{\Psi\Phi} = \sin^2\Psi(\varepsilon_{11} - \varepsilon_{33}) + \varepsilon_{33} + \sin 2\Psi\varepsilon_{13}$$
$$(\varepsilon_{\Psi\Phi} = \sin^2\Psi(\varepsilon_{22} - \varepsilon_{33}) + \varepsilon_{33} + \sin 2\Psi\varepsilon_{23}) \quad (2)$$

The curve $\varepsilon_{\Psi\Phi}$ as a function of $\sin^2\Psi$ is based on the following parameters:

- Intercept $= \varepsilon_{33}$
- Slope $= \varepsilon_{11} - \varepsilon_{33}$ $(\varepsilon_{22} - \varepsilon_{33})$
- Ellipse opening $= \varepsilon_{13}$ (ε_{23})

The values of ε_{33} and $\varepsilon_{22} - \varepsilon_{33}$ along the welded joint are shown in Fig. 7. The ε_{33} intercept exhibits an unusual variation, caused by the superposition of a temperature gradient along the sample and a variable elastic strain. As $\varepsilon_{22} - \varepsilon_{33}$ is not sensitive to the temperature gradient, it provides more robust results. As it can be seen, $\varepsilon_{22} - \varepsilon_{33}$ is constant within the base metal, but exhibits strong variations within the weld metal and the HAZ. In the first case, this reveals that heterogeneities due to the multipass welding are neither fully relieved by post-weld stress annealing nor by creep. In the latter case, we suppose that the variations result from internal stresses due to differences in the plastic behaviour of the base metal, the HAZ and the weld metal. In the following, a particular focus will be paid on the evolution of $\varepsilon_{22} - \varepsilon_{33}$ and $\varepsilon_{11} - \varepsilon_{33}$ along the specimens during the *in situ* tests.

The evolution with time of the elastic strain $\varepsilon_{22} - \varepsilon_{33}$, along the sample (from the base metal to the HAZ) is illustrated in Fig. 8. The strain is averaged over 10 consecutive measurements (*i.e.* 1 mm) in order to reduce experimental noise. For the reference case, without loading, (black line in Fig. 8), the strain values are shifted near 0. Due to some dispersion on the curve $\varepsilon_{\Psi\Phi}$ as a function of $\sin^2\Psi$ for the reference sample, variations in strain values along the specimen are visible but are not significant. For all crept specimens, the strain evolves in a similar way along the welded joint, *i.e.* with a local maximum at the HAZ, bounded by local minima at the boundary with the base metal and the weld metal. Due to the repeatability of the strain evolution on 5 different samples after 5 independent experiments, this strain evolution is significant and characteristic of creep damage on the welded joint.

4. Modelling

4.1. Method

The shape of the specimens is complicated, therefore the development of an analytic solution is difficult for the comparison of stress and strain fields with experimental results. Thus, it is proposed to compute the plastic strain, the total and elastic strain in the whole volume of a model specimen, then to deduce the average $\varepsilon_{22} - \varepsilon_{33}$ (resp. $\varepsilon_{11} - \varepsilon_{33}$) strain along the path of the incident X-ray beam travelling in the $\Phi = 90°$ (resp. $\Phi = 0°$) direction of the X_1X_3 (resp. X_2X_3) middle plane, as shown in Fig. 5b. To further simplify the problem, it is assumed that

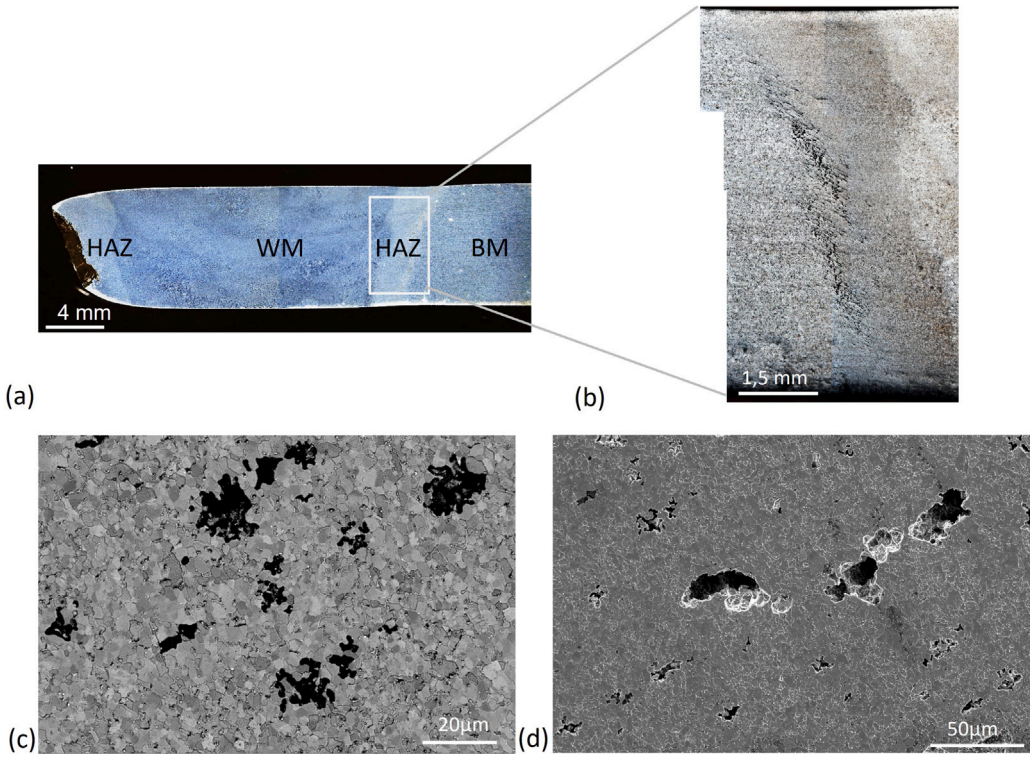

Fig. 6. (a) Optical macrograph of a cross-section along the fractured specimen length, after 5200 h of creep at 600 °C and 100 MPa, (b) zoom in the HAZ, (c)–(d) SEM pictures in the ICHAZ cavity band, in Backscattered-Electron and Secondary Electrons mode, respectively.

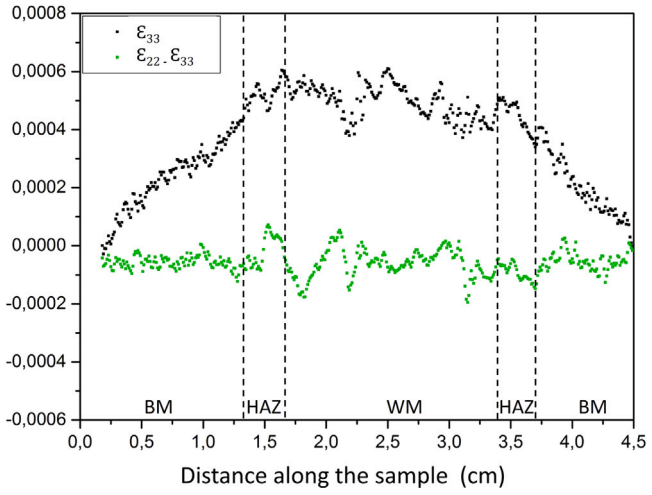

Fig. 7. ε_{33} and $\varepsilon_{22} - \varepsilon_{33}$ evolution along the sample interrupted after 4100 h creep test, experimentally determined by the $\sin^2\Psi$ method.

the constitutive law remains the same for the base metal and the weld metal, while the strain rate of the HAZ is more than double under the same conditions [17].

4.2. FEM simulation

The creep tests were simulated using the Finite Elements Method (FEM) with the Abaqus software package. The creep strain rate was taken as a power law:

$$\dot{\varepsilon_{eq}} = A\left(\frac{\sigma_{eq}}{\sigma_0}\right)^n \tag{3}$$

with σ_{eq} is the Von Mises stress, which is, in the case of isotropic plasticity:

$$\sigma_{eq} = \frac{1}{\sqrt{2}} \times \sqrt{(\sigma_1 - \sigma_2)^2 + (\sigma_2 - \sigma_3)^2 + (\sigma_3 - \sigma_1)^2}. \tag{4}$$

The reference stress is $\sigma_0 = 100$ MPa, and σ_1, σ_2 and σ_3 are the principal stress components. The exponent n of the power law was fixed to $n = 10$ for all welded zones. Meanwhile, Young's modulus at 600 °C is 150 MPa, and Poisson's coefficient is $\nu = 0.3$ for all welded zones. The HAZs were fixed to be 2.5 mm thick, similar to experimental specimens, with a 30° inclination versus the specimen axis. The parameter A was chosen so that the average strain rate is the same as the one measured during stage II off creep (see Fig. 2), for which $A_{\mathrm{BM}} = A_{\mathrm{WM}} = 1.15 \times 10^{-6}$, and the size of the strain step between HAZ and base metal increases with the ratio $A_{\mathrm{HAZ}}/A_{\mathrm{BM}}$. For the first step, the deformed specimen after 4100 h of creep is shown in Fig. 9a, with the expected (and exaggerated) necking in the vicinity of the HAZ. The (different) elastic strains in the median plane of the specimen are plotted in Fig. 9b–d. As it can be seen, a larger plastic strain within the HAZ results in tensile internal stresses in the X_1 and X_2 direction (the elastic strain is less negative than expected from the Poisson ratio only) and compressive stresses within the base metal and the weld metal. The magnitude of the variations of ε_{33} is lower, as these variations result mainly from the limited area reduction at necking and from compatibility stresses at surfaces. Last, the $\varepsilon_{22} - \varepsilon_{33}$ and $\varepsilon_{11} - \varepsilon_{33}$ plots exhibit a stronger contrast.

The variation of the slopes $\varepsilon_{22} - \varepsilon_{33}$ along the specimen axis at t = 4100 h between experimental and simulated values, for the parameters chosen in the previous paragraph, are shown in Fig. 10. The experimental curve is derived from the raw data, which explains the high level of noise. The experimental curve of the weld metal is not plotted, due to the large number of small grains and the presence of gas holes in this area, which increase noise and random variations. In Fig. 10, simulated and experimental curves fit with a good representability of the peak in HAZ.

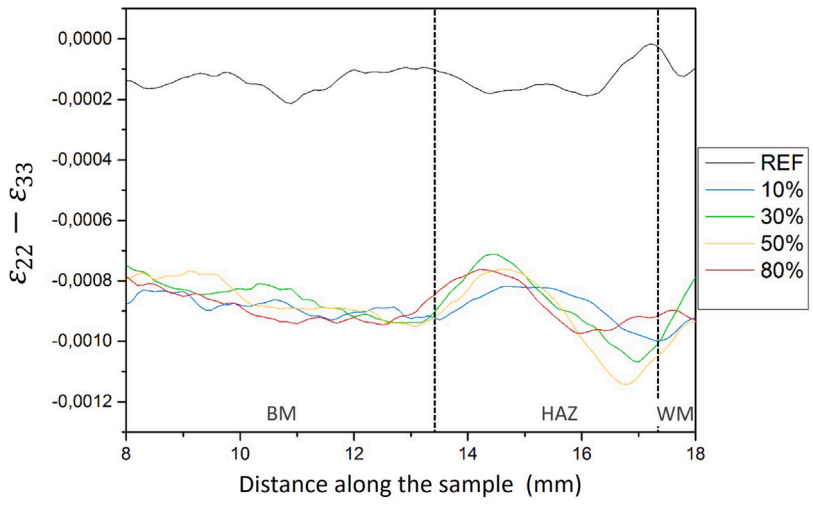

Fig. 8. Strain evolution $\varepsilon_{22} - \varepsilon_{33}$ along the welded joint after creep interrupted test.

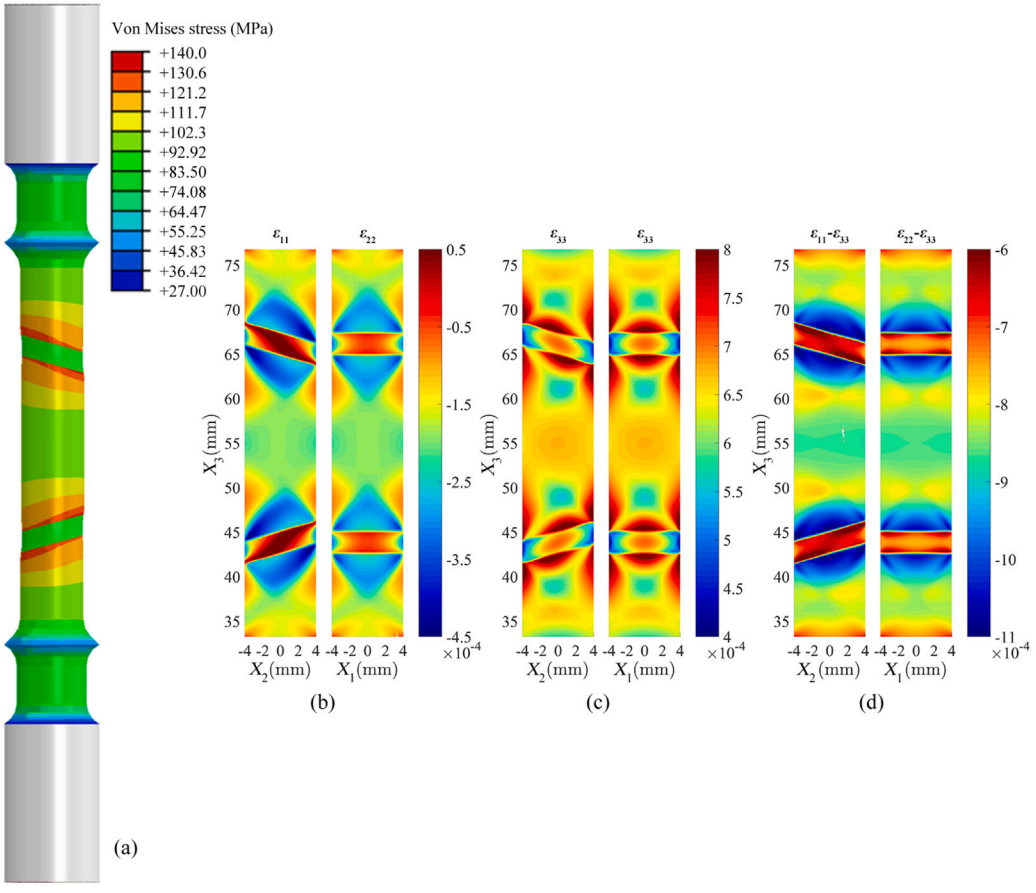

Fig. 9. (a) Von Mises stress, (b)–(d) calculated elastic strains in X_1 (X_2)-X_3 plane of the virtual sample.

The evolution of the step, at the base metal/HAZ interface as a function of creep time, illustrates the damage kinetics of this zone. This evolution is illustrated in Fig. 11, with the comparison of the simulated (red and dashed red lines) and experimental (black line) values. Experimentally, the step at the base metal/HAZ interface is visible from the end of creep stage I, and increases up to 2500 h, *i.e.* in the middle of stage II, and then saturates. In the simulation, the initial HAZ strain rate is chosen to be constant as $A_{\mathrm{HAZ}} = A_{\mathrm{BM}} \times 200$, resulting in stabilisation within a few hours as shown in Fig. 11 by the red dotted line. To obtain a better fit, the parameter A_{HAZ} was allowed to vary with time in order to simulate a gradual softening:

$$A_{\mathrm{HAZ}}(t) = A_{\mathrm{BM}} + A_{\mathrm{HAZ}}(1 - \exp(-t/t_0)) \tag{5}$$

The time constant t_0 was taken as 1000 h and $A_{\mathrm{HAZ}} = A_{\mathrm{BM}} \times 200$. With this gradual softening, the simulated deformation kinetics better fit the experimental one.

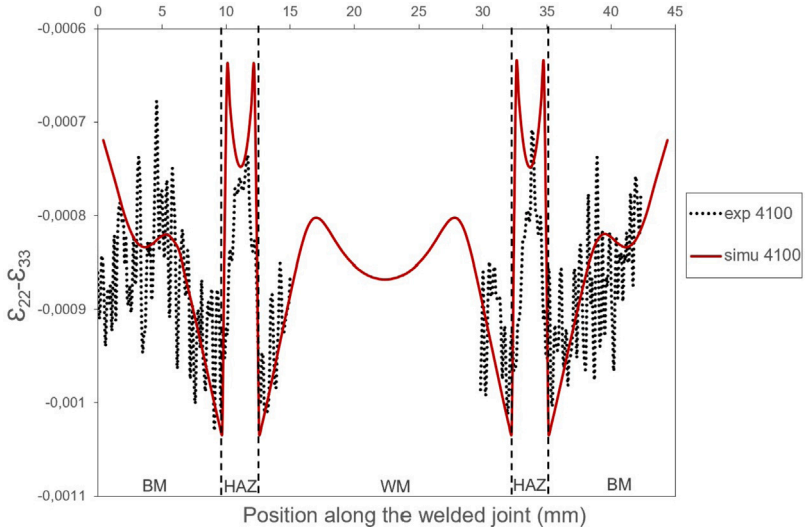

Fig. 10. Experimental (dotted) and calculated (solid line) $\varepsilon_{22} - \varepsilon_{33}$ strain curves after 4100 h.

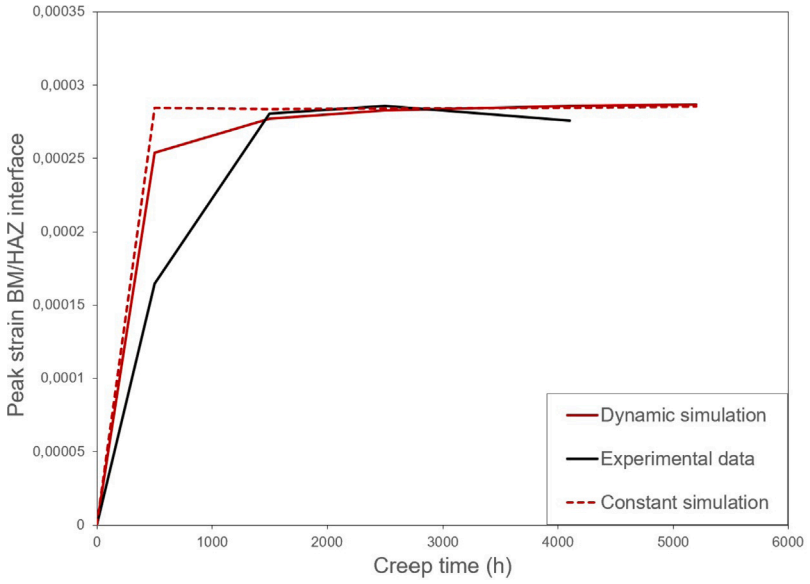

Fig. 11. Step of $\varepsilon_{22} - \varepsilon_{33}$ at the base metal/HAZ interface as a function of creep time for experimental and simulation data. Simulation curves are performed for dynamic (solid line) and constant (dashed line) strain rate. (For interpretation of the references to colour in this figure legend, the reader is referred to the web version of this article.)

5. Discussion

Strain along the weld evolves with a local maximum at the HAZ, bounded by local minima at the interface with the base metal and the weld metal. These experimental results were confirmed by FEM simulations using a power law for the creep strain rate. However, to match the experimental results, the strain rate of the HAZ must be higher than that of the base metal and also variable to follow the kinetics.

The strain evolution is driven by a microstructural softening, which is not constant over the creep time. The nucleation of initial cavities is due to a strong local plasticity related to the softening of the material. Nevertheless, according to the SEM analysis (Fig. 6), the cavities are located in the zone of highest deformation, *i.e.* the ICHAZ, but exclusively in the core of the sample. This phenomenon is also found by the FEM simulations as shown in Fig. 9, the HAZ deforms more than the others, resulting in internal stresses, and the distribution of creep strain on the HAZ varies from the surface towards the centre.

Some authors found that strain concentration and high triaxiality rate affect the distribution of voids [2–4,8]. The triaxiality factor (TF) is the ratio between the hydrostatic stress:

$$\sigma_m = (\sigma_{11} + \sigma_{22} + \sigma_{33})/3 \tag{6}$$

and the Von Mises stress σ_{eq}. TF is thus defined by [8]:

$$\mathrm{TF} = \sigma_m/\sigma_{eq} \tag{7}$$

The distribution of the TF along the welded joint after 4100 h creep is shown in Fig. 12. The sign of the TF depends on the sign of the hydrostatic stress. In our case the TF is positive in tension and negative in compression. The TF is lowest in the HAZ, with a jump at the interfaces with other zones. A large TF favours brittle fracture by cleavage [18], which was observed experimentally in Fig. 6, where cavities and undeformed grains are present. HAZs exhibit maximum creep strain and minimum of the TF, favouring creep damage with cavities in the core of the welded joint.

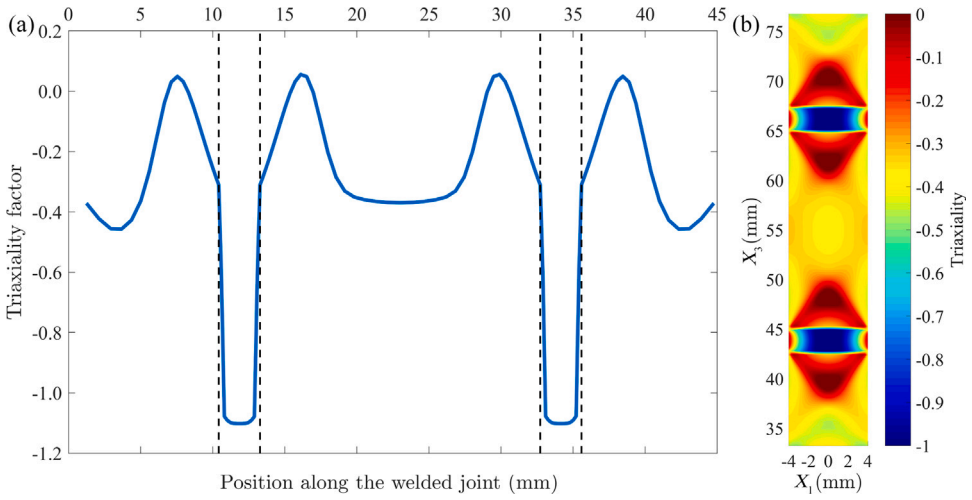

Fig. 12. Simulated TF as a function of position along the welded joint.

6. Conclusion

In-situ testing combined with high energy X-ray diffraction, using synchrotron radiation, allows to determine internal deformations. The strain along the welded joint evolves with a local maximum at the HAZ, limited by local minima at the boundary with the base metal and the weld metal. The difference in strain rate between the HAZ and other welded joint zones results in maximum triaxial stresses in this area. These triaxial stresses are responsible for cavity nucleation and growth in the core of the ICHAZ, further reducing the mechanical strength of the ICHAZ. The combination of cavity formation and recovery of the microstructure [19] leads to severe local softening in the ICHAZ, corresponding to the failure zone.

Declaration of competing interest

The authors declare that they have no known competing financial interests or personal relationships that could have appeared to influence the work reported in this paper.

Data availability

Data will be made available on request.

Acknowledgements

This work has been sponsored by Institut de Soudure through its research centre in Yutz France and l'Institut Carnot ICÉEL. The authors thank Dr. Stéphane Berbenni and Dr. Thiebaud Richeton (LEM3) for fruitful discussions.

References

[1] P.J. Ennis, A. Czyrska-Filemonowicz, Recent advances in creep-resistant steels for power plant applications, Sadhana 28 (2003) 709–730.
[2] M.E. Abd El-Azim, O.H. Ibrahim, O.E. El-Desoky, Long term creep behaviour of welded joints of P91 steel at 650° C, Mater. Sci. Eng. A 560 (2013) 678–684.
[3] T. Watanabe, M. Tabuchi, M. Yamazaki, H. Hongo, T. Tanabe, Creep damage evaluation of 9Cr–1Mo–V–Nb steel welded joints showing Type IV fracture, Int. J. Press. Vessels Pip. 83 (1) (2006) 63–71.
[4] Y. Li, H. Hongo, M. Tabuchi, Y. Takahashi, Y. Monma, Evaluation of creep damage in heat affected zone of thick welded joint for Mod.9Cr–1Mo steel, Int. J. Press. Vessels Pip. 86 (9) (2009) 585–592.
[5] J.A. Siefert, J.D. Parker, Evaluation of the creep cavitation behavior in Grade 91 steels, Int. J. Press. Vessels Pip. 138 (2016) 31–44.
[6] T. Ogata, T. Sakai, M. Yaguchi, Damage characterization of a P91 steel weldment under uniaxial and multiaxial creep, Mater. Sci. Eng. A 510–511 (C) (2009) 238–243.
[7] M.E. Abd El-Azim, OE El-Desoky, H Ruoff, F Kauffmann, E Roos, Creep fracture mechanism in welded joints of P91 steel, Mater. Sci. Technol. 29 (2013) 1027–1033.
[8] Takashi Ogata, Takayuki Sakai, Masatsugu Yaguchi, Damage assessment method of P91 steel welded tube under internal pressure creep based on void growth simulation, Int. J. Press. Vessels Pip. 87 (11) (2010) 611–616.
[9] P. Andersson, L.Å Samuelson, P. Segle, The significance of weldment material mis-matching on stress redistribution and creep cracking of high temperature components, Mater. High Temp. 15 (3–4) (1998) 243–248.
[10] V. Gaffard, J. Besson, A.F. Gourgues-Lorenzon, Modelling high temperature creep flow, damage and fracture behaviour of 9Cr1Mo–NbV steel weldments, Mater. High Temp. 25 (3) (2008) 159–167.
[11] J.P. Feiereisen, O. Ferry, A. Jacques, A. George, Mechanical testing device for in situ experiments on reversibility of dislocation motion in silicon, Nucl. Instrum. Methods Phys. Res. B 200 (2003) 339–345.
[12] J. Kieffer, D. Karkoulis, PyFAI, a versatile library for azimuthal regrouping, J. Phys.: Conf. Ser. 425 (20) (2013) 202012, Publisher: IOP Publishing.
[13] G. Geandier, Relation Entre La Microstructure, L'état Mécanique Et La Fissuration De Cermets Alumine Chrome Élaborés À Partir De Poudres Nanocomposites (Ph.D. thesis), 2002.
[14] B.B He, Two-Dimensional X-Ray Diffraction, John Wiley & Sons, 2009.
[15] F. Heidelbach, C. Riekel, H.R Wenk, Quantitative texture analysis of small domains with synchrotron radiation X-rays, J. Appl. Crystallogr. 32 (1999) 841–849.
[16] M. Gelfi, E. Bontempi, R. Roberti, L.E Depero, X-ray diffraction Debye Ring Analysis for STress measurement (DRAST): a new method to evaluate residual stresses, Acta Mater. Inc 52 (2004) 583–589.
[17] S. Spigarelli, E. Quadrini, Analysis of the creep behaviour of modified P91 (9Cr–1Mo–NbV) welds, Mater. Des. 23 (6) (2002) 547–552.
[18] Nicola Bonora, Gabriel Testa, Andrew Ruggiero, Gianluca Iannitti, Domenico Gentile, Continuum damage mechanics modelling incorporating stress triaxiality effect on ductile damage initiation, Fatigue Fract. Eng. Mater. Struct. 43 (8) (2020) 1755–1768.
[19] S. Collomb, P. Gressel, J. Ghanbaja, A. Jacques, A. Redjaï mia, Characterization of welded joint in martensitic steel Grade 91 after interrupted creep test at 600 ° C, Mater. Sci. Eng. A 855 (2022) 143851.